Cancer Nanotechnology

RESEARCH Open Access

Carbon nanoparticles-Fe(II) complex for efficient theranostics of xenografted colonic tumor

Ping Xie[1], Yuanfang Huang[2], Kexin Tang[2], Xian Wu[3], Cheng Zeng[2], Sheng-Tao Yang[3*] and Xiaohai Tang[2*]

*Correspondence:
yangst@swun.edu.cn;
pharmmateceo@enraypharm.com

[1] State Key Laboratory of Oral Diseases, West China, College of Stomatology, Sichuan University, Chengdu, People's Republic of China
[2] Sichuan Enray Pharmaceutical Sciences Company, Chengdu, People's Republic of China
[3] Key Laboratory of Pollution Control Chemistry and Environmental Functional Materials for Qinghai-Tibet Plateau of the National Ethnic Affairs Commission, School of Chemistry and Environment, Southwest Minzu University, Chengdu 610041, People's Republic of China

Abstract

Background: Overwhelming Fe accumulation in tumor arouses strong oxidative stress. To benefit the cancer patients, Fe(II) delivered by carbon nanoparticles-Fe(II) complex (CNSI-Fe) should be visualized to ensure the successful intratumoral injection and the antitumor mechanisms should be investigated at molecular level.

Results: Intracellular Fe accumulations associating with the uptakes of CNSI-Fe were observed both in vitro and in vivo. The retention of Fe(II) in tumor over 72 h was visualized by magnetic resonance imaging. CNSI-Fe inhibited the tumor growth and expanded the lifespan of colonic tumor-bearing mice. The antitumor activity of CNSI-Fe was attributed to the increases of OH radicals and the oxidative stress in tumor cells, which resulted in cell apoptosis and ferroptosis. The transcriptome analyses confirmed the changes of ferroptosis and inflammation signaling pathways by CNSI-Fe treatment. The low toxicity of CNSI-Fe was indicated by the serum biochemistry, hematology, and histopathology.

Conclusion: CNSI-Fe induced the efficient apoptosis and ferroptosis of colonic tumor for cancer therapy. Our results would benefit the clinical applications of CNSI-Fe and stimulate great interest in the nanomedicine.

Keywords: Carbon nanoparticles, Ferrous iron, Antitumor activity, Ferroptosis, Magnetic resonance imaging

Background

The rapid developments of nanomedicine bring new hope for cancer therapy nowadays (Farjadian et al. 2022; Chang et al. 2021; Abdolahinia et al. 2022; Xu et al. 2022a; Zhang et al. 2023; Huang et al. 2021). Nanomaterials could be applied in drug delivery (Farjadian et al. 2022), immunoadjuvant (Chang et al. 2021), nanoenzyme (Abdolahinia et al. 2022), photothermal therapy (Xu et al. 2022a), photodynamics therapy (Zhang et al. 2023), bioimaging (Huang et al. 2021), and so on. Among these applications, nanomedicine could arouse ferroptosis for cancer treatment (Shen et al. 2023; Chen et al. 2021). For example, the hybrid $CoMoO_4$-phosphomolybdic acid nanosheet (CPMNS) induced the lipid peroxide accumulation, elevated glutathione (GSH) depletion for glutathione

peroxidase 4 (GPX4) enzyme deactivation, and aroused reactive oxygen species (ROS) burst, which resulted in efficient ferroptosis and chemotherapy of 4T1 tumor cells (Wu et al. 2021b). Ke et al. achieved the self-assembly of thiol functionalized Iridium(III) complexes into biodegradable coordination polymeric nanoparticles (NPs) under oxidative conditions (Ke et al. 2022). Upon 720 nm laser irradiation, the NPs generated a mixture of $^1O_2$ and superoxide anion radicals ($^{\cdot}O_2^-$) to induce apoptosis and ferroptosis for tumor inhibition. Luo et al. encapsulated a proteolysis targeting chimera of GPX4 within the ROS-degradable lipid NPs (Luo et al. 2022). Upon the therapy, an enhanced GPX4 degradation and ferroptosis induction in cancer cells were observed both in vitro and in vivo. Another novel demonstration was the delivery of glucose oxidase by its self-assemblies with hydrophobic molecules into NPs to induce ferroptosis of breast cancer (Zhang et al. 2022).

Fe is an essential element for organisms. The lack or overdose of Fe would lead to unwanted toxicity and hazards (Showkat et al. 2019). Overwhelming loading of Fe into tumor is a simple strategy to initiate ferroptosis. Fe-containing NPs are widely applied in ferroptosis therapy. For example, Wang et al. prepared carbonic anhydrase inhibitor (CAI)-modified ferrous sulfide NPs to release CAI, Fe^{2+}, and H_2S, which was suitable for Fe^{2+}-mediated Fenton reaction to initiate ferroptosis for effective tumor elimination (Wang et al. 2022). Liang et al. reported that renal clearable ultra-small single-crystal Fe NPs could efficiently induce tumor cell ferroptosis and immunogenetic cell death (Liang et al. 2021). After functionalizing with iRGD, Fe NPs effectively suppressed the tumor growth, promoted the maturation of dendritic cells, and triggered the adaptive T cell response. Many nanosized delivery systems were reported for Fe ions to induce ferroptosis. For instance, He et al. reported a near-infrared (NIR) light-triggered Fe^{2+} delivery agent (LET-6) (He et al. 2021). Thermal expansion of NPs by laser irradiation triggered the transformation of LET-6 to release Fe^{2+}. Li et al. used metal–organic framework ZIF-8 NPs to deliver Fe^{2+} and the ferroptosis inhibited the growth of MDA-MB-231 cells and tumor (Li et al. 2021).

Although the achievements of nanomedicine are exciting and hopeful, there are several key issues hindering their clinical uses. First, the formulation of nanomedicine is usually very complicated. The production at large scale is difficult. Second, the heterogeneous nature of nanomaterials makes it hard to reach the satisfied uniformity among different batches. Third, the efficient accumulation of nanomedicine in tumor after systemic injection usually requires the use of expensive targeting moieties. Fourth, the toxicity and safety issues of nanomedicine are essential and crucial for the clinical applications. To address these problems, we adopted carbon nanoparticles (CNSI) to load Fe (denoted as CNSI-Fe) into H22 tumor and achieved high antitumor efficiency (Xie et al. 2020). The intratumoral injection solved the tumor accumulation issue, and the good biosafety of carbon allowed the safe applications of CNSI-Fe. Thus, CNSI-Fe is currently under clinical trial evaluations. To benefit the cancer patients, the facile technique is required to ensure the success of intratumoral injection of CNSI-Fe, and the antitumor mechanisms of CNSI-Fe at molecular level are highly demanded.

In this study, we visualized CNSI-Fe by magnetic resonance imaging (MRI) and evaluated the antitumor performance of CNSI-Fe in xenografted colonic tumor-bearing mice. The antitumor activity of CNSI-Fe was evaluated both in vitro and in vivo by measuring

the cell proliferation, tumor growth and survival rates. The Fe accumulations were measured by MRI and inductively coupled plasma mass spectrometry (ICP-MS). The cellular uptakes of CNSI-Fe were investigated by hematoxylin–eosin (HE) staining and transmission electron microscopy (TEM) observations. The antitumor mechanisms were studied by measuring the levels of ROS, oxidative stress, GPX4, Ki67, and caspase-3. The alterations of gene levels were revealed by transcriptome analyses. The toxicity of CNSI-Fe was assayed by serum biochemistry, hematology, and histopathology. The implication to the clinical applications of CNSI-Fe in cancer therapy is discussed.

Methods

Preparation of CNSI-Fe

CNSI-Fe was prepared following our previous protocols with some modifications. Briefly, poloxamer (0.0600 g) was dissolved in 20 mL of water. After adding C40 carbon powder (2.0 g), the mixture was homogenized for 10 min and submitted to ultra-high-pressure homogenizer for treatments of three times at 20, 000 psi. The as-prepared black suspension was CNSI. $FeSO_4{\cdot}7H_2O$ (1.490 g) was dissolved in 20 mL of water and the pH was adjusted to 2.8. The solution was injected to vials of 91 mg $FeSO_4{\cdot}H_2O$ each for lyophilization to obtain $FeSO_4{\cdot}H_2O$ powder. Before injection, $FeSO_4{\cdot}H_2O$ was dissolved in CNSI at designed concentrations by simple mixing. The mixture was lyophilized to obtain CNSI-Fe powder for the characterizations by TEM (Autoflex, Bruker, Bonn, Germany), Raman spectroscopy (Renishaw inVia plus, Renishaw, Wotton-under-Edge, UK), Infrared spectroscopy (IR, Tensor27, Bruker, Germany), X-ray photoelectron spectroscopy (XPS, Axis Ultra, Kratos, Manchester, UK), and dynamic light scattering (DLS, Zetasizer Nano ZS90, Malvern Instruments, Malvern, UK).

Antitumor evaluations of CNSI-Fe in vitro

The CT26.WT cells were inoculated into 6-well plates at 1.0×10^5 cells/well. After incubation at 37 ℃ under 5% CO_2 flow for 24 h, the cells were exposed to CNSI-Fe at Fe concentrations of 3.1–200 μg/mL and the cells without exposure were taken as the control. After another 48-h incubation, the cell proliferation was measured by counting the cell numbers under optical microscope.

To investigate the antitumor mechanisms, the cells exposed to CNSI-Fe (100 μg/mL) were compared with the control cells. First, the cells were digested with 5.0 mL of HNO_3 in a microwave digestion system at 180 °C for 30 min. The as-obtained solution was diluted with 0.1% HNO_3 for ICP-MS measurements (ICAP RQ, ThermoFisher Scientific Co., USA). Second, the mitochondrial membrane potentials were measured by JC-1 kit following the kit instruction (100 T, Beijing Solarbio Technology Co., LTD, Beijing, China). Third, the cells were repeatedly frozen-thawed and the lysates were subjected to electron spin-resonance spectroscopy (ESR) measurements (JES-FA200, JEOL, Japan) after adding with 5,5-dimethyl-1-pyrroline-N-oxide (DMPO). Forth, the GPX4 and long train acyl-CoA synthetases 4 (ACSL4) levels were measured by Wuhan Servicebio Technology Co. using the Western blot method following literature protocols (Zhou et al. 2022). The representative images of GPX4 and ACSL4 are presented in Supplementary materials (Additional file 1: Fig. S1). Finally, the ultrastructure of cells was investigated

by TEM after the fixation and ultra-thin section following standard protocols (Additional file 1: Fig. S2) (Liang et al. 2021).

Accumulations of CNSI-Fe in vivo

The animal experiments were checked and approved by the Ethics Committee of Southwest Minzu University and performed in accordance with the Animal Care and Use Program Guidelines of the Sichuan Province, China. BALB/c mice were inoculated with 0.1 mL of CT26.WT cell suspension (3.0×10^7 cells) on the right upper limb. After 7 d, the tumor volume reached 100–150 mm^3 and the tumor was injected with 50 μL of CNSI-Fe (Fe concentration of 15 mg/mL). The accumulation of CNSI-Fe in tumor was monitored by MRI before and after the injection at 15 min, 24 h, and 72 h (MRI: BioSpec 70/30USR, Bruker, Germany). Separately, CNSI-Fe solutions at 15, 7.5, 3.75, 1.88, 0.94, and 0.47 mg/mL were imaged by MRI.

The Fe contents of serum and tissues were measured by ICP-MS for pharmacokinetics and biodistribution. Tumor-bearing mice were injected with 50 μL of CNSI-Fe (Fe concentration of 15 mg/mL) and the blood samples were collected at 2 min–24 h. The serum samples were prepared from the blood samples by centrifugation at 1800 g and 4 ℃ for 10 min. The serum (30 μL) was added with 0.1% of Triton and 0.1% of HNO_3. After mixing for 1 min, the solution was subjected to ICP-MS (8900, Agilent Technologies Inc., California, USA). The serum Fe contents were subjected to one-compartment model for pharmacokinetics analysis. For biodistribution, the mice were sacrificed at 15 min, 24 h, and 72 h. The tissues were collected, digested and diluted with 0.1% of Triton and 0.1% HNO_3 for ICP-MS measurements. In addition, the tumor tissues were fixed, ultra-thin sectioned, and negatively stained for TEM observations.

Antitumor evaluations of CNSI-Fe in vivo

BALB/c mice were inoculated with 0.1 mL of cell suspension (3.0×10^7 cells) on the right upper limb. After 7 d, the tumor volume reached 100–150 mm^3 and the tumor was injected with 50 μL of saline (control group), 50 μL of CNSI (50 mg/mL), 50 μL of CNSI-Fe (Fe concentrations of 3.8 mg/mL, CNSI-Fe L group), 50 μL of CNSI-Fe (Fe concentrations of 7.5 mg/mL, CNSI-Fe M group), and 50 μL of CNSI-Fe (Fe concentrations of 15 mg/mL, CNSI-Fe H group). The cis-dichlorodiammineplatinum(II) (DDP) group was intraperitoneally injected with DDP at 5 mg/kg. The injection was performed twice at day 0 and day 3. The tumor volumes were measured three times a week. After 14 d, the mice were sacrificed and the tumors were dissected for weighting. The tumor tissues were fixed with 10% formaldehyde for HE staining. The tumor tissues were also fixed with 2.5% glutaraldehyde for ultra-thin section and the negative staining was performed for TEM sampling. Separately, the mice were raised until the mice died, the tumor volume reached 2000 mm^3, or the bodyweight lost over 20% to calculate the survival rates.

To investigate the antitumor mechanisms of CNSI-Fe, the tumor tissues were collected and homogenized. The 10% homogenates were added with DMPO for ESR measurements. The 10% homogenates were analyzed by using the oxidative stress kits following the producer's instructions, including H_2O_2, peroxidase (POD), GSH, and malondialdehyde (MDA). The tumor tissues were fixed by 10% formaldehyde and sent to Wuhan Servicebio Technology Co. for immunohistochemical analyses of caspase-3 and Ki67. The

GPX4 levels were measured by Wuhan Servicebio Technology Co. using Western blot method (Liang et al. 2021). The representative images of caspase-3, Ki67, and GPX4 were presented in Supplementary materials (Additional file 1: Fig. S3). The tumor samples of control, CNSI and CNSI-Fe H group were flash-frozen in liquid nitrogen and transferred to a − 80 ℃ refrigerator before transcriptome measurements. The transcriptome analyses were performed using an Illumina HiSeqTM at Majorbio Bio-Pharm Technology Co., Ltd. (Shanghai, China). The data were checked against the KEGG database to identify significantly enriched KEGG pathways at a false discovery rate (FDR) < 0.05. When the corrected *P* value (*p*-adjust) was less than 0.05, it was considered that the KEGG PATHWAY function was significantly enriched. The pathway ID was obtained by KEGG functional annotation analysis. The data mining and figure presentation are all implemented on the online platform of Majorbio Cloud Platform (www.Majorbio.com).

Biosafety evaluations of CNSI-Fe

The toxicity of CNSI-Fe was evaluated at 14 d post-injection. The blood samples were collected for biochemical analyses (serum) and hematological analyses (whole blood) on an automatic biochemical analyzer (Chemray 800, Rayto, China) and an automatic blood cell analyzer (BC-2800vet, Mindray, China). The liver, spleen, heart, and kidney samples were collected, fixed with 10% formaldehyde, and processed following HE staining protocols. The histopathological changes were checked under optical microscope (Eclipse Ci-L, Nikon, Japan).

Statistical analysis

All data were expressed as the mean with the standard deviation (mean ± SD). The difference was considered significant when $p < 0.05$, which was calculated by one-way ANOVA test.

Results and discussion

Characterization of CNSI-Fe

CNSI-Fe was black suspension that was composed by small carbon nanoparticles and Fe^{2+} ions. Under TEM, the carbon particles were recognized with an average diameter of about 25 nm (Fig. 1a). The aggregates of particles were loosely packed. The carbon particles contained sp^2 carbon in form of graphite carbon as indicated by the G-band at 1590 cm^{-1} in Raman spectrum (Fig. 1b). The disorder of graphite structure was reflected by the D-band at 1350 cm^{-1}. The oxygen-containing groups on carbon particles and polyvinylpyrrolidone (PVP) chains were presented in the IR spectrum (Fig. 1c). In the aqueous suspension, the hydrodynamic radium of CNSI-Fe was 190 nm, consistent with the aggregation under TEM (Fig. 1d). The characterization data were consistent with the previous report (Xie et al. 2020). It is worthy to note that the aforementioned preparation protocols of CNSI-Fe have been established in Good Manufacturing Practice (GMP) workshop, which produces 10,000 packages of CNSI-Fe once (containing 91 mg $FeSO_4 \cdot H_2O$ in each package).

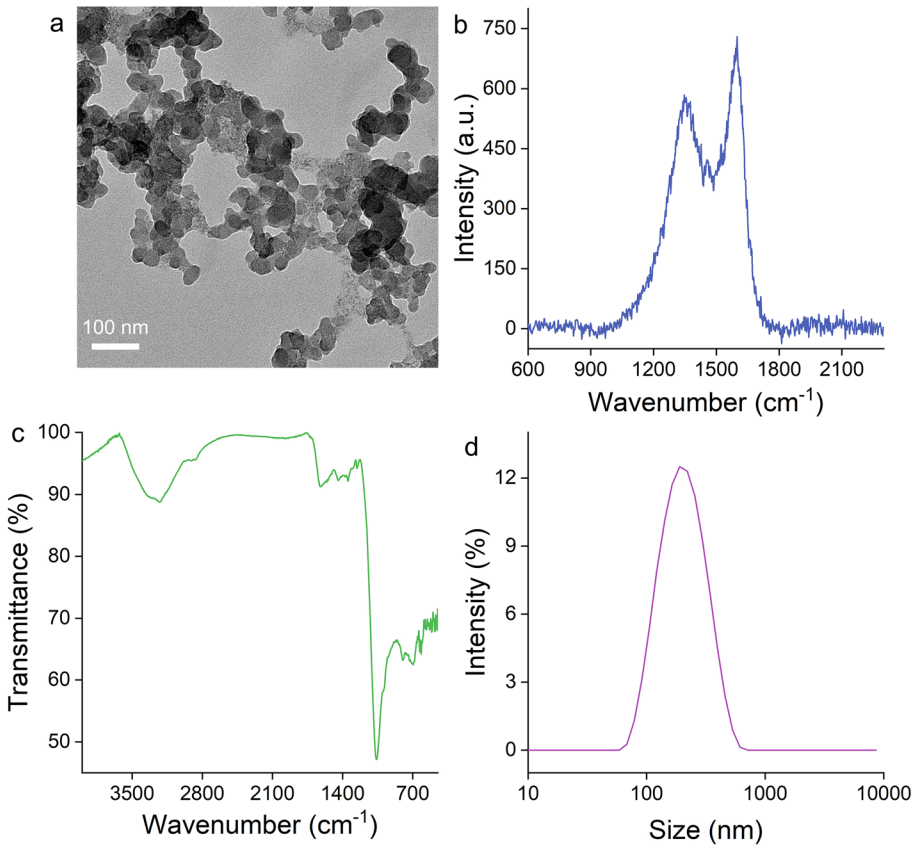

Fig. 1 Characterization of CNSI-Fe. **a** TEM image. **b** Raman spectrum. **c** IR spectrum. **d** DLS spectrum

Antitumor activity of CNSI-Fe in vitro

The antitumor activity of CNSI-Fe was evaluated in vitro on CT26.WT cells. The dose-dependent inhibition of cell proliferation was observed in the range of 3.1–200 μg/mL. At 12.5 μg/mL, the viability of CT26.WT cells was 60% of the control. The cell proliferation decreased to 22% of the control at 200 μg/mL. Considering the nontoxic nature of CNSI particles (Xie et al. 2017), the inhibition of cell proliferation should be attributed to the Fe uptakes, since significant increase of Fe content was observed. At 100 μg/mL, the Fe content reached 1324 ± 161 ng/10^6 cells, much higher than that of the control (480 ± 105 ng/10^6 cells) and CNSI group (484 ± 92 ng/10^6 cells). Similarly, Chen et al. reported the delivery of Fe^{2+}/Fe^{3+} ions by polydopamine NPs to tumor cells and the enhanced Fe uptakes led to the loss of cell viability via ferroptosis (Chen et al. 2019). In our study, the Fe accumulation lowered the mitochondrial membrane potential (Fig. 2c) and generated more hydroxyl radicals (Fig. 2d). The Fe accumulation and ROS generation obviously would induce ferroptosis of CT26.WT cells, which was reflected by the decrease of GPX4 level after the incubation with CNSI-Fe (Fig. 2e). However, ACSL4 level kept unchanged. Ultrastructural changes of CT26.WT cells were observed under TEM. The number of mitochondria increased and some of them became smaller. The expansion and break of rough endoplasmic reticulum occurred. The number of autolysosomes increased. Some xenobiotic particles

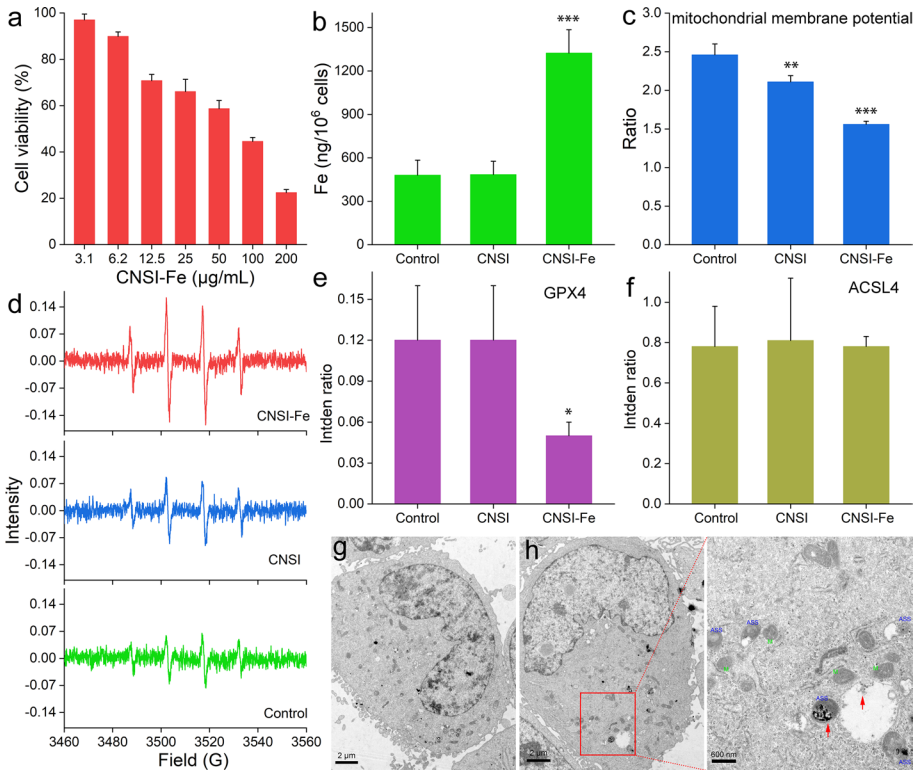

Fig. 2 Antitumor activity of CNSI-Fe to CT26.WT cells in vitro. **a** Cell proliferation. **b** Intracellular Fe contents. **c** Mitochondrial membrane potentials. **d** Hydroxyl radical generations. **e** GPX4 levels. **f** ACSL4 levels. **g** TEM image of control group. **h** TEM image of the cell exposed to CNSI-Fe. ASS means autolysosome, M means mitochondria, and the red arrows indicate the xenobiotic particles. * $p < 0.05$, ** $p < 0.01$, *** $p < 0.001$ comparing to the control group

were found intracellular, which should be assigned to CNSI particles. For better comparison, more TEM images were included in Supplementary materials (Additional file 1: Fig. S2). These data collectively indicated that CNSI-Fe was taken by CT26.WT cells to induce ferroptosis and resulted in cell viability loss.

Antitumor activity of CNSI-Fe in vivo

The intratumoral injection is a common used method in oncological surgery during the clinical applications of CNSI for lymph node mapping. The advantage of intratumoral injection over other dosing pathways is the high tumor accumulation rate (Francis et al. 2020). There is strong demand for clinical doctors to visualize the Fe^{2+} during the intratumoral injection to ensure the successful injection. The MRI imaging of overloading of Fe in tissues has been reported in the literature (Hernando et al. 2014). For instance, MRI was applied in quantifying liver iron in patients. Herein, we found that CNSI-Fe had strong T2 signal under MRI (Fig. 3). The higher CNSI-Fe resulted in darker images of MRI by shortening the transverse relaxation time, due to the paramagnetism nature of Fe^{2+}. The T2 signal should be attributed to Fe^{2+} ions, since CNSI did not alter the T2 signal. The corresponding transverse relaxation rate R_2 of Fe^{2+} was 1.92 $mM^{-1}{\cdot}s^{-1}$. Thus, T2 images could reflect the distribution of Fe in tumor. Before the injection, the

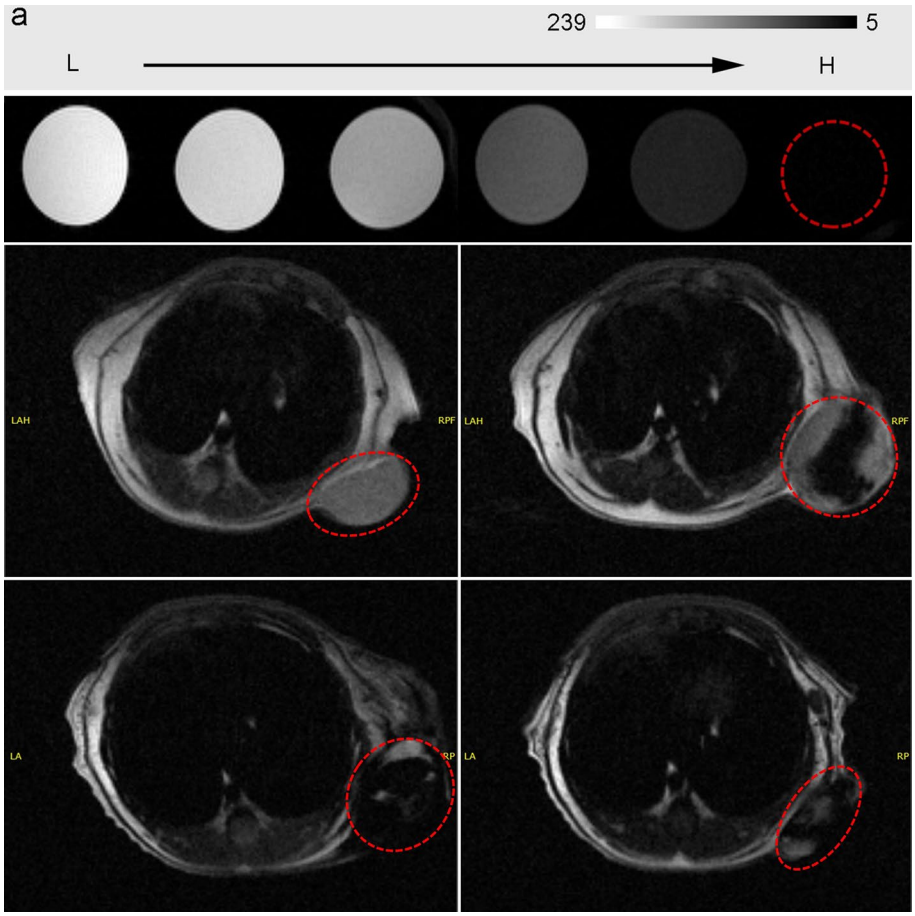

Fig. 3 MRI images of CNSI-Fe in solution and after the injection in vivo. **a** CNSI-Fe in solution. **b** Control group. **c** After the injection of CNSI-Fe at 15 min. **d** After the injection of CNSI-Fe at 24 h. **e** After the injection of CNSI-Fe at 72 h

tumor was bright under MRI. After the injection of CNSI-Fe, the tumor became dark and the brighter skin surrounded the dark area. At 24 h, the darkness of tumor area kept unchanged, indicating the retention of Fe in tumor. At 72 h, there was slight decrease of T2 signal, but the tumor was still dark, suggesting that CNSI-Fe retained over 72 h. There were slight differences among these MRI sections, because the mice were taken out after each imaging evaluation to raise in cages. The MRI results indicated that CNSI-Fe was successfully injected to tumor and retained for a long period. MRI is a mature technology in clinical treatments; thus, it could offer a method for the doctors to verify the success of intratumoral injection without additional learning.

The accumulation of Fe in tumor was further confirmed by ICP-MS measurements. There was an increase of serum Fe from 4.2 ± 0.4 μg/mL (control) to 41 ± 14 μg/mL at 2 min post-injection of CNSI-Fe (Fig. 4a), which should be due to the diffusion of Fe ions from tumor into capillary and finally into the blood circulation. The serum Fe decreased gradually along with time elapse and recovered to normal levels after 8 h. The half-life time ($t_{1/2}$) of serum Fe was 6.7 h. The increase of serum Fe in short term should be well considered during the clinical applications. Currently, the deferoxamine is adopted as an emergency treatment for patients during the clinical trials. The Fe ions entering the

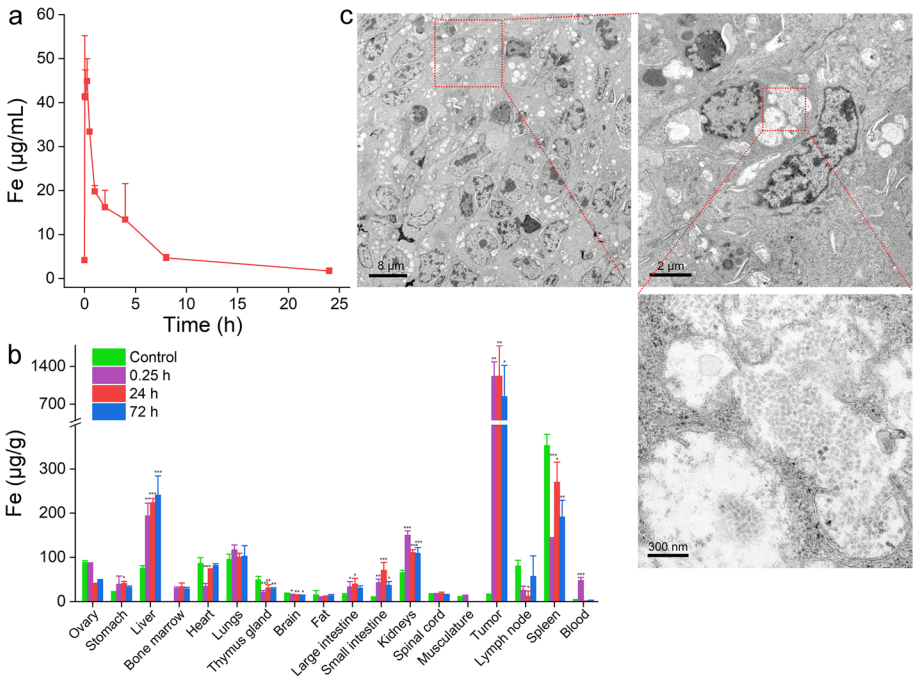

Fig. 4 Bioaccumulation of Fe in vivo. **a** Blood Fe contents. **b** Biodistribution of Fe. **c** TEM images of tumor tissue injected with CNSI-Fe. * $p < 0.05$, ** $p < 0.01$, *** $p < 0.001$ comparing to the control group

blood circulation were cleared slowly and accumulated majorly in liver (Fig. 4b). Comparing to the control, the Fe contents increased largely in liver, stomach, intestine, and kidneys. In liver, the Fe content was 76 ± 6 μg/g for the control and the value increased to 194 ± 29 μg/g at 0.25 h. The hepatic Fe content further increased to 241 ± 43 μg/g at 72 h. The increases of Fe contents in intestine should be attributed to the excretion of hepatic Fe, which was mainly excreted through bile secretion. Small portion of hepatic Fe could be excreted through urine, thus explained the renal Fe increases. Most importantly, tumors had significant and persistent Fe accumulations. The control had a Fe content of 16 ± 1 μg/g and the values were 1215 ± 270 μg/g at 0.25 h post-injection. The Fe content did not change at 24 h (1219 ± 555 μg/g). The Fe content decreased to 840 ± 577 μg/g after 72 h, which was still 52 times of the control. The overwhelming Fe accumulations in tumor could generate ROS for cancer therapy (He et al. 2020). In addition, the accumulation of CNSI-Fe in tumor was verified by TEM observation (Fig. 4c). The particulates in phagosomes were clearly recognized and attributed to carbon particles. Under TEM, the nuclear membrane, cell membrane, and organelles became vague, suggesting the damage of cellular structures by CNSI-Fe.

The persistent accumulation of CNSI-Fe in tumor could inhibit the tumor growth. The tumor growth of control group was the fastest among the 6 groups (Fig. 5a). CNSI groups showed slight inhibiting effect. The typical anticancer drug DDP showed effective inhibition of tumor growth. At 14 d, the tumor volume was 1550 ± 306 mm^3, corresponding to an inhibition efficiency of 59.5%. CNSI-Fe showed dose-dependent efficiencies in tumor therapy. CNSI-Fe L group (0.19 mg Fe/mouse) had similar efficiency as DDP group. CNSI-Fe M group (0.38 mg Fe/mouse) inhibited the tumor growth more and the inhibition efficiency was 77.3%. At 0.75 mg Fe/mouse, CNSI-Fe H group showed potent

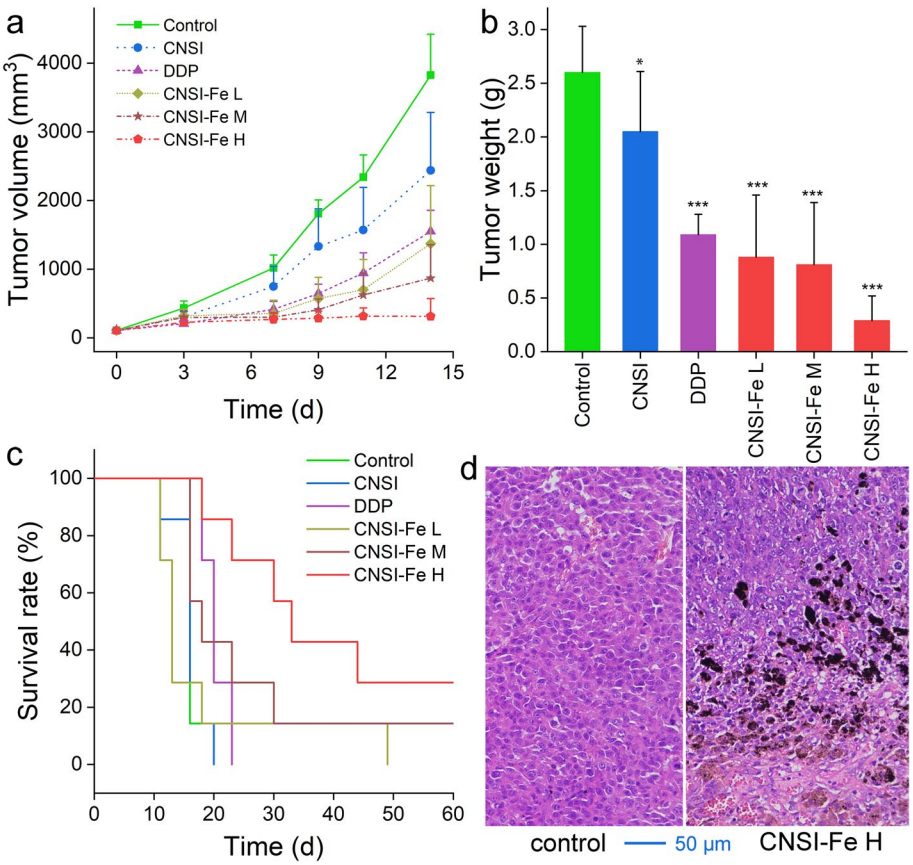

Fig. 5 Inhibition of tumor growth by CNSI-Fe. **a** Tumor volumes. **b** Tumor weights. **c** Survival rates. **d** HE staining images. * $p < 0.05$, ** $p < 0.01$, *** $p < 0.001$ comparing to the control group

therapeutic effects on tumor. The tumor volume was only 313 ± 259 mm^3, corresponding to an inhibition efficiency of 91.8%. The impressive efficiency of CNSI-Fe for colonic tumor inhibition was confirmed by the lowered tumor weights and the prolonged survival times. After the mice were sacrificed, the tumors were weighted and the inhibition efficiencies were calculated following the sequence of CNSI (21%) < DDP (58%) < CNSI-Fe L (66%) < CNSI-Fe M (69%) < CNSI-Fe H (89%) (Fig. 5b). CNSI-Fe had meaningful benefits to the survival rates, too. After 20 d, all mice in the control group and CNSI group died (Fig. 5c). DDP group had a survival rate of 28.6% at 20 d and all died at 23 d. CNSI-Fe L group was slightly better, while CNSI-Fe M and H groups survived even at 60 d. The survival rate of CNSI-Fe M group was 14.3% at 60 d and the value was 28.6% for CNSI-Fe H group. The good therapeutic effect of CNSI-Fe was also reflected by the HE staining images (Fig. 5d). The black substances were attributed to CNSI particles and the necrosis of tumor was observed in the CNSI-Fe group.

Antitumor mechanisms of CNSI-Fe

The antitumor mechanism of CNSI-Fe should be due to the ferroptosis according to the in vitro results (Fig. 2). To verify this hypothesis in vivo, we measured several ferroptosis-related indicators. First, the overwhelming accumulation of Fe in tumor generated

lots of hydroxyl radicals (Fig. 6a). Weak signal of ·OH was detected in CNSI group and no radicals were found in the control group. CNSI-Fe group had strong OH signal, indicating the generation of hydroxyl radicals. The generation of hydroxyl radicals lasted for 14 d, suggesting the persistent therapeutic effects of CNSI-Fe. This well explained the efficient inhibition of tumor growth for 14 d (Fig. 5a). CNSI did not arouse oxidative damage to tumor, while CNSI-Fe induced serious oxidative damage even after 14 d (Fig. 6b). The H_2O_2 level increased to 323 ± 174% of the control, which could be decomposed into hydroxyl radicals by Fe^{2+} via Fenton reaction (Xu et al. 2022b; Xiang et al. 2022; Xie et al. 2022). The POD and GSH levels were up-regulated by CNSI-Fe, which should be regarded as the stimulation of antioxidative responses. MDA is a typical indicator of lipid peroxidation. The MDA increased to 475 ± 55% of the control, indicating the meaningful oxidative damage. GPX4 is a typical indicator of ferroptosis. However, the GPX4 increased from 0.67 ± 0.14 of the control group to 1.43 ± 0.98 of the CNSI-Fe group. This might be regarded as a stress reaction against ROS generation. Typically, when organisms face oxidative stress, they would up-regulate the antioxidative systems to alleviate the damage. At this stage, the up-regulations of GPX4, POD, and GSH were reasonable (Guo et al. 2021). When the organisms could not handle the oxidative stress, these parameters would go down as indicators of oxidative damages. Immunohistochemical technology is more conducive to directly display the expression and distribution of tumor tissue-related proteins. In future, the GPX4 levels might be quantified by immunohistochemical stain. Ki67 increase was observed, too. Ki67 is an indicator of cell proliferation, which meant that the remnant tumor cells that survived during the treatment had higher proliferation. Another ferroptosis-related issue was apoptosis. The increased GPX4 and Ki67 might imply that those tumor cells survived during the CNSI-Fe treatment might be more tolerable against the oxidative radicals. The good news was that these tumor cells would be surgically removed in clinical applications, because

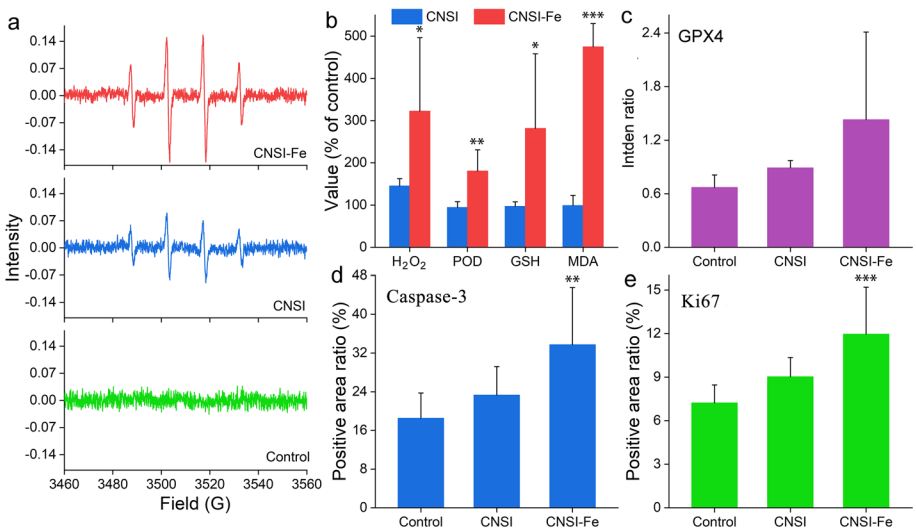

Fig. 6 Molecular mechanisms for the antitumor activity of CNSI-Fe. **a** Hydroxyl radicals. **b** Oxidative stress. **c** GPX 4 levels. **d** Ki67 levels. **e** Caspase-3 levels. * $p < 0.05$, ** $p < 0.01$, *** $p < 0.001$ comparing to the control group

CNSI-Fe was designed to shrink the tumor to reach the tumorectomy requirements. The increased caspase-3 level of CNSI-Fe group confirmed the apoptosis after CNSI-Fe treatment. These indicators and the Fe content data (Fig. 4) collectively suggested that CNSI-Fe induced the Fe accumulations in tumor to initiate ferroptosis.

To reveal the molecular mechanism as illustrated in Fig. 7a, the transcriptome analysis of tumor tissue after the treatment of CNSI-Fe was performed. Through KEGG enrichment analysis of different gene functions (CNSI group VS Control group), CNSI had low impact on the function rich gene, as indicated by the small numbers of different function rich gene (Additional file 1: Fig. S4a). The mild function enrichments were mainly in IL-17 signaling, tumor cell necrosis factor signaling, and NF-kB signaling pathways, which were related to inflammation and cell death. In contrast, CNSI-Fe treatment had much higher impact on the function rich gene (Fig. 7b). The functional enrichments were mainly manifested in peroxidase proliferator-activated receptors (PPARs) signaling pathway, regulation of fat decomposition in adipocytes, cytokine cell receptor, and Ca^{2+} signal pathway. PPARs are closely associated with energy metabolism, growth, and development of tumor cells. Nuclear receptor co-activators cooperate with PPAR–retinoid X receptor (RXR), supplement, and stabilize active transcriptional complexes, which regulate lipid metabolism, fat formation, maintain metabolic stability and the

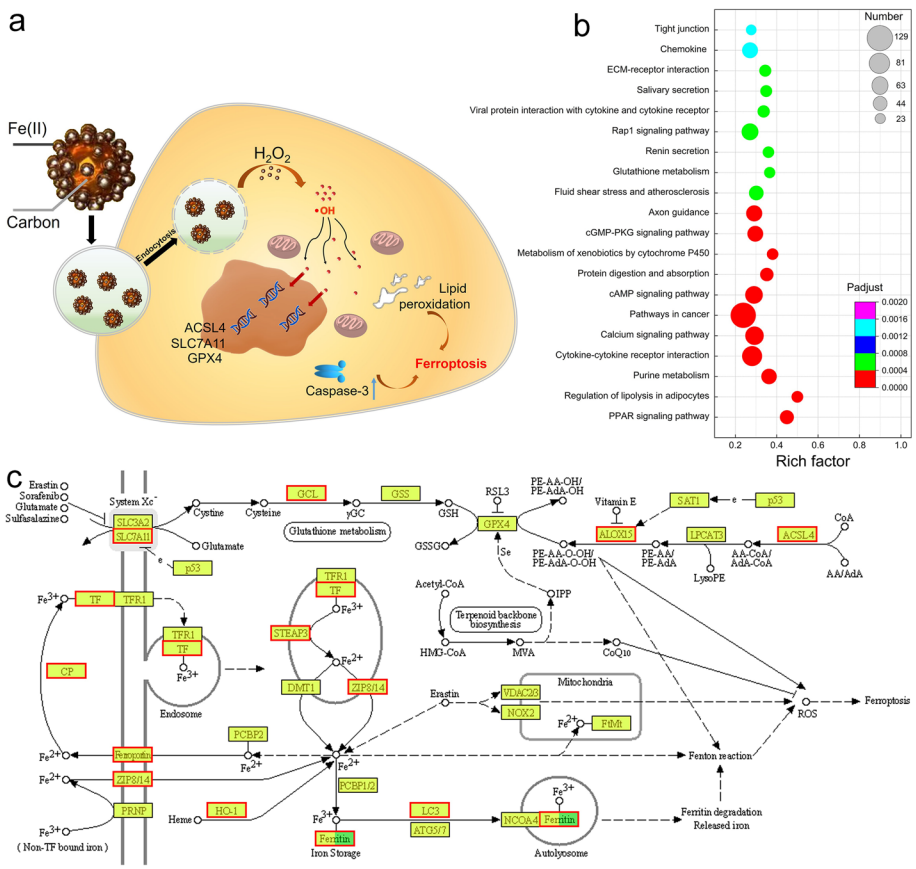

Fig. 7 Transcriptome analysis of tumor tissue after the treatment of CNSI-Fe. **a** Schematic illustration of antitumor mechanism. **b** KEGG functional enrichment. **c** Ferroptosis signaling pathway diagram

expression of inflammation genes, and induce anticancer effect in a variety of tumor cells. Fat decomposition regulation-related genes were significantly enriched and the expression level was significantly up-regulated, which provided energy for the body and maintained the cell vital signs. Cytokine cell receptor and Ca^{2+} signaling pathways are involved in the development of tumor cells. Cytokine is involved in cell signal transduction. Interferon (INF) and transforming growth factor-β (TGF-β) can directly inhibit the growth of tumor cells. IFN-γ, interleukin-2 (IL-2), IL-12, and IL-15 enhance the cytotoxicity of lymphocytes and bone marrow cells, thereby inhibiting tumor growth. Neutralizing mAb or receptor antagonists targeting key inflammatory cytokines have anticancer activity. In addition, tumor cells secrete factors that cause NF-kB activity. Blocking NF-kB can stop the proliferation of tumor cells. Thus, the changes of function rich genes could explain the antitumor activities of CNSI-Fe. In the KEGG functional enrichment analyses, the mice injected with CNSI-Fe showed up-regulated ACSL4 gene, which is an iron death-related gene in the ferroptosis pathway of tumor cells. SLC7A11 was compensatorily elevated, while GPX4 had no significant change (Fig. 7c). The gene GPX4 in the glutathione metabolism pathway had no significant change, either (Additional file 1: Fig. S4b). The changes of GPX4 gene could be regarded as a stress response of tumor cells to radical attack. The unchanged GPX4 gene and up-regulation of GPX4 activity might suggested that the response of GPX4 to CNSI-Fe was through protein level rather than gene level. Genes GPX2, GPX3, and GPX7 were significantly up-regulated in the pathway of arachidonic acid metabolism (Additional file 1: Fig. S4a).

Biosafety of CNSI-Fe

Beyond the excellent therapeutic efficiency, CNSI-Fe held another merit in cancer therapy as the acceptable biosafety. CNSI-Fe treatment induced the alanine aminotransferase (ALT) and aspartate aminotransferase (ALP) increases, while aminotransferase (AST) level decreased (Fig. 8a). These changes should be assigned to the Fe toxicity to hepatic function (Tenenbein 2001; Xiong et al. 2022), considering the increased hepatic Fe accumulations (Fig. 4b) and nontoxic nature of CNSI (Xie et al. 2017). In our previous evaluation, Fe(II) alone induced the decreases of ALT and AST, and the increase of ALP was observed (Xie et al. 2020). CNSI-Fe had some influence on the hematology, too (Fig. 8b). CNSI-Fe slightly increased the red blood cell (RBC) and hemoglobin (HGB). The platelet (PLT) value increased significantly. During the chemotherapy of tumor, RBC and PLT usually decrease, which is the side effect of chemotherapy (Wu et al. 2021a; Liu et al. 2019). CNSI-Fe increased these parameters, suggesting the good biosafety of CNSI-Fe to blood circulation. On the other hand, the inhibition of immune cells is also a typical side effect of chemotherapy (Zitvogel et al. 2008). The white blood cell (WBC), lymphocyte (Lymph), monocytes (Mon), and neutrophilic granulocyte (Gran) decreased after CNSI-Fe treatment. This suggested that CNSI-Fe lowered the immune cells and induced the immunotoxicity. In addition, CNSI-Fe had limited influence on the histopathological characteristics of liver, spleen, kidneys, and heart (Fig. 8c). The HE images of liver spleen, kidneys, and heart of CNSI-Fe group were similar as those of control group. Thus, CNSI-Fe only induced functional changes to liver, but no organic damage was induced. The toxicity of CNSI-Fe was mainly from Fe overdosages, which might be treated by deferoxamine during the clinical applications (Tenenbein 1996).

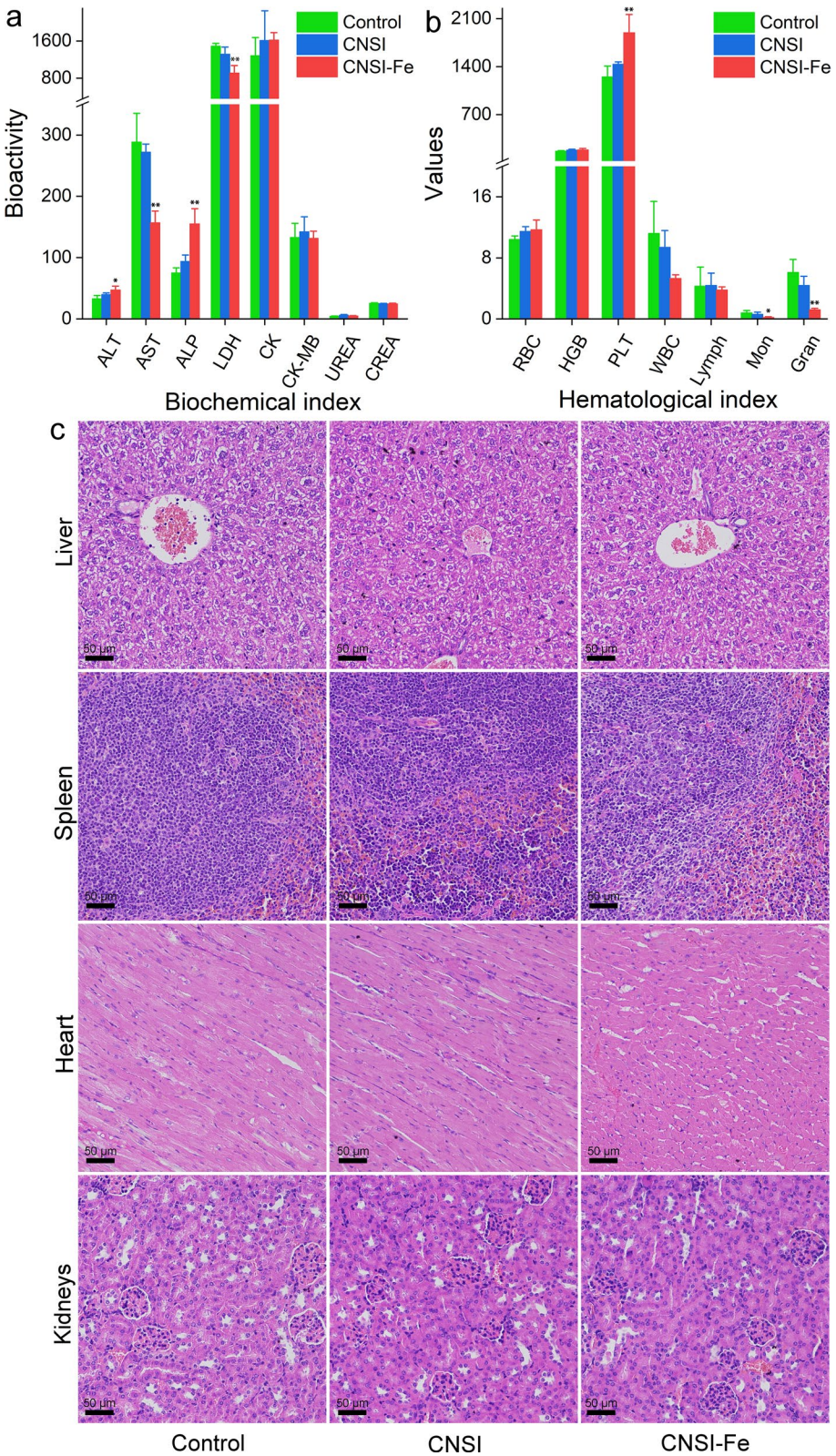

Fig. 8 Biosafety evaluations of CNSI-Fe. **a** Serum biochemical parameters. **b** Hematological analyses. **c** Histopathological observations of liver, spleen, heart, and kidneys. * $p < 0.05$, ** $p < 0.01$ comparing to the control group

Conclusions

In summary, CNSI-Fe showed high antitumor activity for the therapy of colonic cancer, where the success of intratumoral injection of CNSI-Fe was visualized by MRI. The efficient loading of Fe in tumor cells induced ferroptosis as evidenced by the Fe accumulation, apoptosis, and oxidative stress along with the GPX 4 increase and the ferroptosis signaling pathway disturbance. The low toxicity of CNSI-Fe ensured its safe applications. Our results extended the usages of CNSI-Fe in cancer therapy and would hopefully provide a facile theranostics tool for doctors. We believe that CNSI-Fe will benefit cancer patients in future after the ongoing clinical trials.

Supplementary Information

The online version contains supplementary material available at https://doi.org/10.1186/s12645-023-00196-5.

Additional file 1: Figure S1. Representative Western blot images for GPX4 and ACSL4 in Fig. 2. **Figure S2.** Additional TEM images of the control group and the cells exposed to CNSI-Fe. **Figure S3.** Representative Western blot images for GPX4 and immunohistochemical staining images for caspase-3 and Ki67 in Fig. 6. **Figure S4.** Transcriptome analysis of tumor tissue after the treatment of CNSI or CNSI-Fe.

Acknowledgements

The authors acknowledge the assistance of analytical instruments from Key Laboratory of General Chemistry of the National Ethnic Affairs Commission, Southwest Minzu University.

Author contributions

PX performed the biological experiments and wrote the original draft. YH performed the cell experiments and participated in writing the original draft. KT involved in the biological experiments and performed the analytical characterization. XW performed the analytical characterization. CZ prepared the samples. STY conceptualized, supervised the study, and edited the manuscript. XT conceptualized, administrated the project, and reviewed the manuscript. All the authors read and approved the final manuscript.

Authors' information

Kexin Tang is a student intern from Emory College of Arts and Sciences, Emory University.

Funding

This study was supported by the Fundamental Research Funds for the Central Universities, Southwest Minzu University (No. ZYN2022002).

Availability of data and materials

All data generated or analyzed during this study are included in this published article and its supplementary information file.

Declarations

Ethics approval and consent to participate

All animal care protocols and experiments in this study were approved by the Ethics Committee of Southwest Minzu University.

Consent for publication

Not applicable.

Competing interests

The authors declare no conflict of interests.

Received: 24 February 2023 Accepted: 11 April 2023
Published online: 19 April 2023

References

Abdolahinia ED, Fathi M, Pirdel Z, Jafari S, Samiei M, Adibkia K et al (2022) Strategies to improve drug penetration into tumor microenvironment by nanoparticles: focus on nanozymes. OpenNano 8:100100

Chang M, Hou Z, Wang M, Li C, Lin J (2021) Recent advances in hyperthermia therapy-based synergistic immunotherapy. Adv Mater 33(4):2004788

Chen L, Lin Z, Liu L, Zhang X, Shi W, Ge D et al (2019) Fe^{2+}/Fe^{3+} ions chelated with ultrasmall polydopamine nanoparticles induce ferroptosis for cancer therapy. ACS Biomater Sci Eng 5(9):4861–4869

Chen X, Kang R, Kroemer G, Tang D (2021) Broadening horizons: the role of ferroptosis in cancer. Nat Rev Clin Oncol 18(5):280–296
Farjadian F, Roointan A, Mohammadi-Samani S, Hosseini M (2022) Mesoporous silica nanoparticles: synthesis, pharmaceutical applications, biodistribution, and biosafety assessment. Chem Eng J 439:135661
Francis DM, Manspeaker MP, Schudel A, Sestito LF, O'Melia MJ, Kissick HT et al (2020) Blockade of immune checkpoints in lymph nodes through locoregional delivery augments cancer immunotherapy. Sci Transl Med 12(563):3575
Guo Y, Du J, Xiao C, Xiang P, Deng Y, Hei Z et al (2021) Inhibition of ferroptosis-like cell death attenuates neuropathic pain reactions induced by peripheral nerve injury in rats. Eur J Pain 25(6):1227–1240
He Y, Liu X, Xing L, Wan X, Chang X, Jiang H (2020) Fenton reaction-independent ferroptosis therapy via glutathione and iron redox couple sequentially triggered lipid peroxide generator. Biomaterials 241:119911
He T, Yuan Y, Jiang C, Blum NT, He J, Huang P et al (2021) Light-triggered transformable ferrous ion delivery system for photothermal primed chemodynamic therapy. Angew Chem Int Ed 60(11):6047–6054
Hernando D, Levin YS, Sirlin CB, Reeder SB (2014) Quantification of liver iron with MRI: state of the art and remaining challenges. J Magn Reson Imaging 40(5):1003–1021
Huang M, Gu Z, Zhang J, Zhang D, Zhang H, Yang Z et al (2021) MXene and black phosphorus based 2D nanomaterials in bioimaging and biosensing: progress and perspectives. J Mater Chem B 9(26):5195–5220
Ke L, Wei F, Xie L, Karges J, Chen Y, Ji L et al (2022) A biodegradable Iridium(III) coordination polymer for enhanced two-photon photodynamic therapy using an apoptosis-ferroptosis hybrid pathway. Angew Chem Int Ed 61(28):e202205429
Li Z, Wu X, Wang W, Gai C, Zhang W, Li W et al (2021) Fe(II) and tannic acid-cloaked MOF as carrier of artemisinin for supply of ferrous ions to enhance treatment of triple-negative breast cancer. Nanoscale Res Lett 16(1):37
Liang H, Wu X, Zhao G, Feng K, Ni K, Sun X (2021) Renal clearable ultrasmall single-crystal Fe nanoparticles for highly selective and effective ferroptosis therapy and immunotherapy. J Am Chem Soc 143(38):15812–15823
Liu B, Wang W, Fan J, Long Y, Xiao F, Daniyal M et al (2019) RBC membrane camouflaged Prussian blue nanoparticles for gamabutolin loading and combined chemo/photothermal therapy of breast cancer. Biomaterials 217:119301
Luo T, Zheng Q, Shao L, Ma T, Mao L, Wang M (2022) Intracellular delivery of glutathione peroxidase degrader induces ferroptosis in vivo. Angew Chem Int Ed 61(39):e202206277
Shen F, Fang Y, Wu Y, Zhou M, Shen J, Fan X (2023) Metal ions and nanometallic materials in antitumor immunity: function, application, and perspective. J Nanobiotechnol 21:20
Showkat A, Bhat DS, Hassan T, Majid S (2019) Heavy metal toxicity and their harmful effects on living organisms-a review. Int J Med Sci Diag Res 3(1):106–122
Tenenbein M (1996) Benefits of parenteral deferoxamine for acute iron poisoning. J Toxicol Clin Toxicol 34(5):485–489
Tenenbein M (2001) Hepatotoxicity in acute iron poisoning. J Toxicol Clin Toxicol 39(7):721–726
Wang J, Sun Z, Wang S, Zhao C, Xu J, Gao S et al (2022) Biodegradable ferrous sulfide-based nanocomposites for tumor theranostics through specific intratumoral acidosis-induced metabolic symbiosis disruption. J Am Chem Soc 144(43):19884–19895
Wu J, Wang Q, Dong X, Xu M, Yang J, Yi X et al (2021a) Biocompatible AIEgen/p-glycoprotein siRNA@reduction-sensitive paclitaxel polymeric prodrug nanoparticles for overcoming chemotherapy resistance in ovarian cancer. Theranostics 11(8):3710–3724
Wu C, Liu Z, Chen Z, Xu D, Chen L, Lin H et al (2021b) A nonferrous ferroptosis-like strategy for antioxidant inhibition–synergized nanocatalytic tumor therapeutics. Sci Adv 7(39):eabj8833
Xiang S, Fan Z, Ye Z, Zhu T, Shi D, Ye S et al (2022) Endogenous Fe^{2+}-activated ROS nanoamplifier for esterase-responsive and photoacoustic imaging-monitored therapeutic improvement. Nano Res 15(2):907–918
Xie P, Yang ST, He T, Yang S, Tang X (2017) Bioaccumulation and toxicity of carbon nanoparticles suspension injection in intravenously exposed mice. Int J Mol Sci 18:2562–2576
Xie P, Yang ST, Huang Y, Zeng C, Xin Q, Zeng G et al (2020) Carbon nanoparticles–Fe(II) complex for efficient tumor inhibition with low toxicity by amplifying oxidative stress. ACS Appl Mater Interfaces 12(26):29094–29102
Xie W, Zhang G, Guo Z, Lu J, Ye J, Xu W et al (2022) Ultra-sensitive iron-doped palladium nanocrystals with enhanced hydroxyl radical generation for chemo-/chemodynamic nanotherapy. Adv Funct Mater 32(12):2107518
Xiong H, Zhang C, Han L, Xu T, Saeed K, Han J et al (2022) Suppressed farnesoid X receptor by iron overload in mice and humans potentiates iron-induced hepatotoxicity. Hepatology 76(2):387–403
Xu W, Wang T, Qian J, Wang J, Hou G, Wang Y et al (2022a) Fe(II)-hydrazide coordinated all-active metal organic framework for photothermally enhanced tumor penetration and ferroptosis-apoptosis synergistic therapy. Chem Eng J 437:135311
Xu F, Chai B, Liu Y, Liu Y, Fan G, Song G (2022b) Superior photo-Fenton activity toward tetracycline degradation by 2D α-Fe_2O_3 anchored on 2D g-C_3N_4: S-scheme heterojunction mechanism and accelerated Fe^{3+}/Fe^{2+} cycle. Colloids Surf A 652:129854
Zhang Y, Jiang S, Lin J, Huang P (2022) Antineoplastic enzyme as drug carrier with activatable catalytic activity for efficient combined therapy. Angew Chem Int Ed 61(41):e202208583
Zhang Q, Luo Q, Liu Z, Sun M, Dong X (2023) Nano-ROS-generating approaches to cancer dynamic therapy: lessons from nanoparticles. Chem Eng J 457:141225
Zhou Z, Liang H, Yang R, Yang Y, Dong J, Di Y et al (2022) Glutathione depletion-induced activation of dimersomes for potentiating the ferroptosis and immunotherapy of "cold" tumor. Angew Chem Int Ed 61(22):e202202843
Zitvogel L, Apetoh L, Ghiringhelli F, Kroemer G (2008) Immunological aspects of cancer chemotherapy. Nat Rev Immunol 8(1):59–73

Publisher's Note